APPLIED SCIENCES AND ENGINEERING

Large-scale, robust mushroom-shaped nanochannel array membrane for ultrahigh osmotic energy conversion

Chao Li[1], Liping Wen[2,3], Xin Sui[1], Yiren Cheng[1], Longcheng Gao[1]*, Lei Jiang[1,2,3]

The osmotic energy, a large-scale clean energy source, can be converted to electricity directly by ion-selective membranes. None of the previously reported membranes meets all the crucial demands of ultrahigh power density, excellent mechanical stability, and upscaled fabrication. Here, we demonstrate a large-scale, robust mushroom-shaped (with stem and cap) nanochannel array membrane with an ultrathin selective layer and ultrahigh pore density, generating the power density up to 22.4 W·m^{-2} at a 500-fold salinity gradient, which is the highest value among those of upscaled membranes. The stem parts are a negative-charged one-dimensional (1D) nanochannel array with a density of ~10^{11} cm^{-2}, deriving from a block copolymer self-assembly; while the cap parts, as the selective layer, are formed by chemically grafted single-molecule–layer hyperbranched polyethyleneimine equivalent to tens of 1D nanochannels per stem. The membrane design strategy provides a promising approach for large-scale osmotic energy conversion.

INTRODUCTION

The osmotic energy existing between the seawater and river water is a large-scale renewable and sustainable energy source, which can be converted to electricity directly by reverse electrodialysis (RED) (*1*–*3*). In the RED systems, one of the most important parts is the ion-selective transport membrane. However, the conventional membranes show poor power density due to their high resistance. To increase the energy conversion ability, two typical approaches have been developed. The first one is the nanopores. Single nanopores indicate ultrahigh power density by decreasing the membrane thickness (*4*–*7*). Continuous effort is devoted to expanding to multipore membranes with high pore density, but the crucial mechanical problem is still unsolved (*8*, *9*). The other approach is the bioinspired nanochannel membranes (BNMs). They are made by physical combination of two separated membranes, acting the roles of selective layer and supporting layer, respectively (*10*–*12*). The BNMs realize high output power density by increasing the effective pore density and decreasing the membrane thickness. However, the membrane (especially the selective layer) thickness minimization is limited by the mechanical problem (typically on the scale of hundreds of nanometers or even bigger). On the other hand, the nanochannel density maximization is restricted by the mismatch between the nanochannels with different diameters and periodic sizes (typically in the range of 10^6 to 10^{10} cm^{-2}). Further increasing the nanochannel density is limited for the reason of mechanical failure. None of previously reported membranes meets all the crucial demands of ultrahigh power density, excellent mechanical stability, and upscaled fabrication.

In nature, electric eels can generate action potential as high as 600 V, owing to the large number of the electrocytes stacked in their bodies. In the electrocytes exist densely packed ion channels, which are chemically and geometrically asymmetric (*13*–*15*). Taking a Cl^- channel as an example, amide nitrogen atoms from amino acids gather together to form an electrostatically favorable narrow tunnel as the Cl^- ion–selective filter, with an extremely short length of about 1.2 nm (*15*). The remainder of the channel is wider and has negative charges provided by the carboxylate groups from glutamate side chains (*16*, *17*). The asymmetric ion channels, exhibiting unidirectional ion transport (*18*), can be analogized to the semiconductor diodes. It is known that the short diodes have much higher diffusion current than that of long diodes (*19*). Similarly, the extremely thin selective filter in the Cl^- channel contributes to the rapid ion diffusion, which must be a key factor for the high power density (*20*). These features inspire us to design the next generation of short ionic diode membranes for high osmotic energy conversion.

In this work, we demonstrate an ultrahigh-density mushroom-shaped nanochannel array membrane with an ultrathin selective layer on a large scale. The nanochannels are composed of two parts: The stem parts are a negative-charged one-dimensional (1D) nanochannel array with a density of ~10^{11} cm^{-2}, deriving from a block copolymer (BCP) self-assembly; the cap parts are positive-charged three-dimensional (3D) channel networks formed by single-molecule–layer hyperbranched polyethyleneimine (h-PEI), equivalent to tens of 1D nanochannels per stem. The total areal density of the nanopores in the selective layer reaches up to ~10^{12} cm^{-2}. The extremely high density of ion channels exhibits unidirectional ion transport and excellent ion selectivity, leading to high-performance energy conversion. The output power density is up to 22.4 W·m^{-2} at a 500-fold salt gradient, which is the highest value among those upscaled membranes. Notably, the membrane fabrication is well-controlled, without sacrificing the upscale and mechanical stability. The membrane design strategy provides a promising approach for large-scale osmotic energy conversion.

RESULTS

Membrane design strategy and fabrication

The nanochannel array membrane is realized by a bottom-up approach (Fig. 1, A to C, and fig. S1). First, a thin film with high-density hexagonally packed cylinders is self-assembled (SA) by a BCP (Fig. 1D

[1]Laboratory of Bio-inspired Smart Interfacial Science and Technology of Ministry of Education, School of Chemistry, Beihang University, Beijing 100191, P. R. China. [2]Key Laboratory of Bio-inspired Materials and Interfacial Science, Technical Institute of Physics and Chemistry, Chinese Academy of Sciences, Beijing 100190, P. R. China. [3]School of Future Technology, University of Chinese Academy of Sciences, Beijing 100049, P. R. China.
*Corresponding author. Email: lcgao@buaa.edu.cn

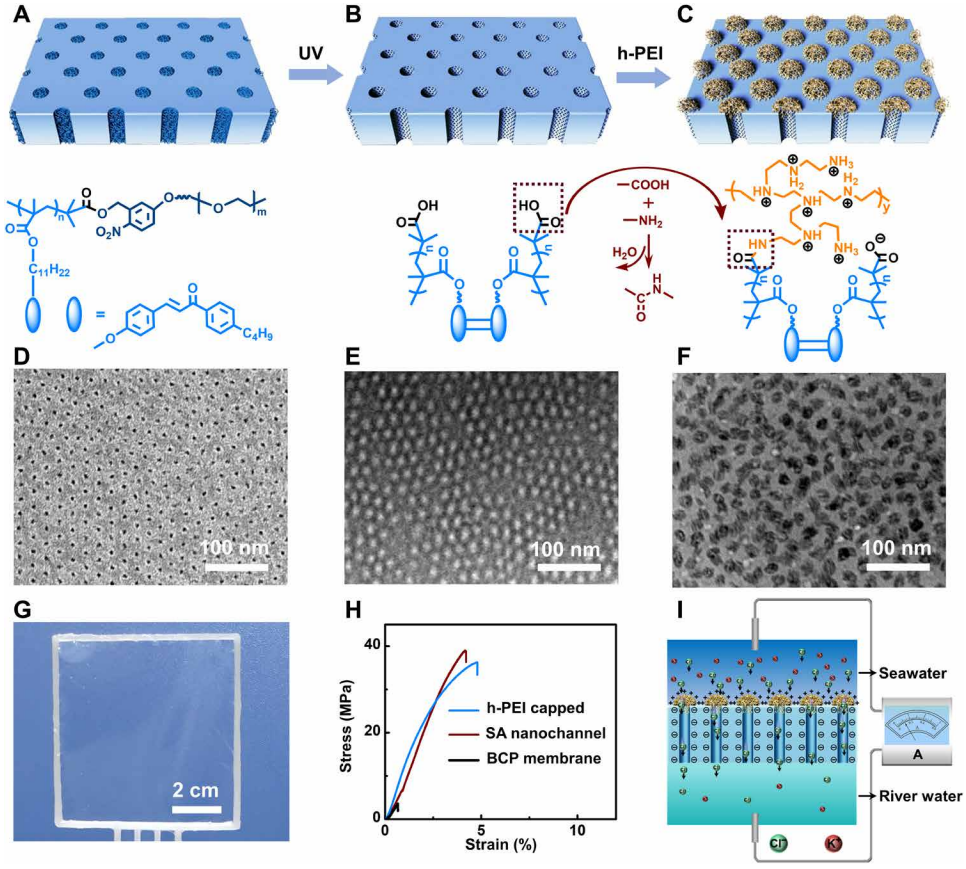

Fig. 1. Nanochannel array membrane for osmotic power generator. (**A**) BCP molecular structure and SA nanostructure. (**B**) The formation of nanochannels by UV treatment. (**C**) The formation of robust h-PEI–capped nanochannels by amidation reaction. Only h-PEI amino groups that contact with the nanochannel surface react with the carboxylate groups. (**D**) TEM image of the BCP SA membrane, showing the hexagonally packed cylinder structure. (**E**) TEM image of the nanochannel array membrane, showing the hexagonally packed nanochannel structure. (**F**) TEM image of the h-PEI–capped membrane, indicating the successful modification. (**G**) The photograph of a large-scale free-standing membrane (>50 cm^{-2}), indicating scalable fabrication and excellent mechanical property. (**H**) Stress-strain curves of the SA membrane before and after UV treatment, as well as the h-PEI–capped membrane, exhibiting highly enhanced mechanical strength after UV cross-linking. (**I**) Illustration of the osmotic energy conversion based on the h-PEI–capped nanochannel membrane. Photo credit: Chao Li, Beihang University.

and figs. S2 to S4). The BCP contains ultraviolet (UV)–cross-linkable chalcone groups and an UV-cleavable o-nitrobenzyl ester (ONB) linker. Second, the nanochannel array structure is formed by UV treatment. During this step, the chalcone-containing blocks cross-link and the ONB linker groups cleave with the in situ generation of carboxylate groups (*21*). Transmission electron microscopy (TEM) and atomic force microscopy (AFM) confirm hexagonally packed nanochannels (Fig. 1E and fig. S5), with the diameter of ~8.4 nm and center-to-center distance of 18.2 nm (fig. S6). Notably, hexagonally packed nanopores are seen on the back side of the membrane, and transmembrane nanochannels are observed from the cross section image (fig. S7). The areal density of the nanochannels is ~10^{11} cm^{-2}. Third, the nanochannels are one-end–modified with single-molecule–layer h-PEI to form mushroom-shaped nanochannels in a robust way. h-PEI contains abundant amino groups, offering reaction sites and providing the highest positive-charge density when protonated (*22*). h-PEI is spin-coated onto the nanochannel membrane surface, and h-PEI fully covers the surface. The used h-PEI has a hydrodynamic diameter of ~19.4 nm (fig. S8), much bigger than the nanochannel diameter (8.4 nm). Thus, h-PEI blocks the entryways instead of entering into the nanochannels (*23*, *24*). Meanwhile, carboxylate groups only exist on the nanochannel surface. Thus, only h-PEI amino groups that contact with the nanochannel surface react with the carboxylate groups, while the unreacted h-PEI is easily washed away by water. As a result, the chemical specificity and steric recognition allow the formation of h-PEI caps on the nanochannels. TEM image provides the evidence for the successful modification, as isolated dark domains covering the nanochannels (Fig. 1F). Nitrogen element appears on the h-PEI–modified side, while no nitrogen is detected on the other side from the x-ray photoelectron spectroscopy spectra (fig. S9). Besides, the membrane exhibits Janus-like zeta potentials and wettability (figs. S10 and S11). On the cap side, the surface shows more positive potential and hydrophilic wettability, due to the presence of h-PEI. While on the other side, the surface shows more negative potential and is slightly hydrophobic, due to the carboxyl groups on the nanochannel surface. The mechanical strength of the membrane after UV treatment is markedly enhanced, and the membrane can be self-standing on a large scale (Fig. 1, G and H). The fabricated membrane is mounted into a two-compartment cell as a separator to evaluate the osmotic energy conversion performance (Fig. 1I).

Ultrahigh-density nanochannels

The ultrahigh density of nanochannels is theoretically analyzed. The h-PEI adapts a 3D conformation with a lot of void space, as simulated by Materials Studio (fig. S12). In aqueous solution, the h-PEI void space is filled with water, i.e., so-called swollen process. As shown on the AFM images, the average height increases from 5.0 to 12.5 nm after swelling (see Fig. 2, A and B, and fig. S13). The local volume fraction (ϕ) of h-PEI in the cap is about ~0.06, exceeding the critical overlap concentration ϕ^* (~10^{-3}) while being much lower than 1 ($\phi^* < \phi << 1$), which can be regarded as semidilute condition (*25*). The h-PEI chains interpenetrate with each other, forming a 3D network–like structure composing of densely packed correlation volumes. These correlation volumes provide ion transport pathways. The correlation length ξ, i.e., the average distance between two overlap points of the chains, is calculated according to the de Gennes' scaling argument (*25*)

$$\xi \approx b\phi^{-\frac{\upsilon}{3\upsilon-1}} \quad (1)$$

where b is the repeating unit size (~0.31 nm). ϕ is the volume fraction of h-PEI. υ is an exponent and it is $\upsilon = 3/5$ under good solvent condition. The correlation length ξ is calculated to be ~2.4 nm.

Since h-PEI is grafted onto the end of the nanochannels, mushroom-shaped 1D-3D hybrid nanochannels are formed (Fig. 2C). To simplify the model, the ions are hypothesized to transport in straight 1D nanochannels, which are integrated in parallel and connected in series with the stem nanochannels. The diameter equals to the PEI correlation length ξ (~2.4 nm). The number of equivalent 1D cap nanochannels is estimated as

$$n \propto \left(\frac{D}{\xi}\right)^2 \quad (2)$$

where D is the average distance between the stem nanochannels (~18.2 nm). Thus, the number of 1D nanochannels in each cap is on the order of 10. The areal density of the stem nanochannels is on the scale of ~10^{11} cm^{-2}, equal to that of the original SA nanostructure. Thus, the total areal density of 1D-1D hybrid nanochannels, constructed by positive-charged 1D cap nanochannels and negative-charged stem nanochannels, reaches ~10^{12} cm^{-2} (Fig. 2C).

Unidirectional ion transport

The ultrahigh-density nanochannel membrane exhibits unidirectional ion transport. As shown in Fig. 2D, the ion transport through the h-PEI–capped nanochannel membrane exhibits a diode-like feature. The current value under positive potential is much bigger than that of under negative potential. In contrast, the membrane with symmetric nanochannels shows linear and ohmic current-voltage (*I-V*) curves. The asymmetric nanochannels, similar to p-n semiconductor junctions, can accumulate or deplete ions efficiently (*26*–*28*). Under positive bias, the anions (Cl^-) preferentially transport from bulk solution into the positive h-PEI nanochannels. Meanwhile, the cations (K^+) preferentially transport from bulk solution into the negative BCP nanochannels. The diffusion of cations and anions forms an ion-enrichment region that results in a higher ionic conductivity. Under a negative bias, ion transport proceeds in the opposite direction. The ion migration from bulk solution into nanochannels is blocked due to electrostatic repulsion, causing an ion-depletion region and leading to a lower ionic conduction (fig. S14). The rectification-ratio

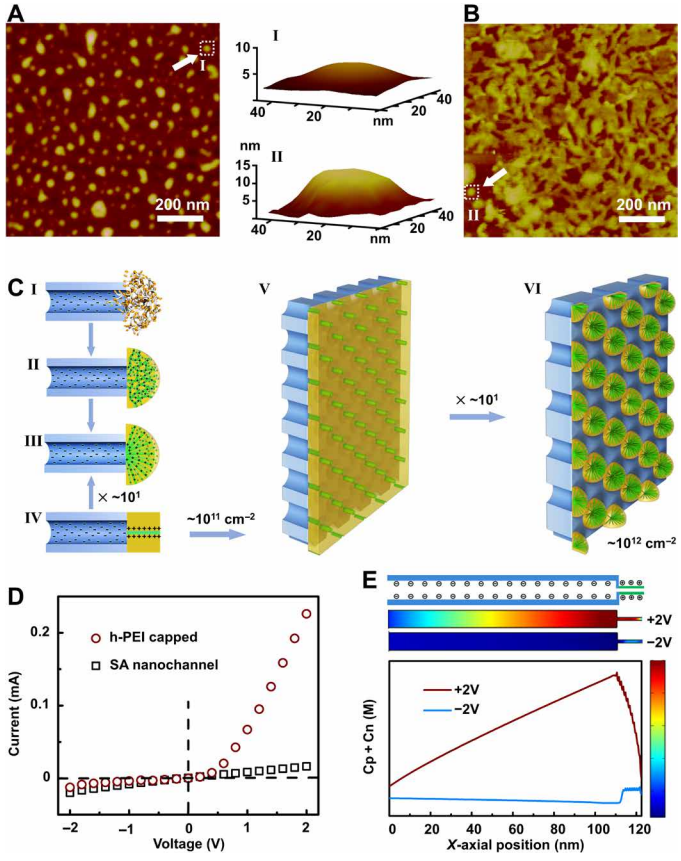

Fig. 2. Ultrahigh-density mushroom-shaped nanochannel array membrane. (**A**) AFM height image of the h-PEI–capped nanochannel membrane surface in air. h-PEI caps collapse with average height of 5.0 nm (I). (**B**) AFM height image of the h-PEI–capped nanochannel membrane surface in aqueous solution. h-PEI caps are swollen with an average height of 12.5 nm (II). (**C**) The schematic illustration of mushroom-shaped nanochannels. The mushroom-shaped nanochannel is composed of the stem and the cap (I). The cap is a 3D network (II), which is simplified into tens of 1D nanochannels (III and IV). The density of arrayed stems is ~10^{11} cm^{-2} (V), and the density of asymmetric 1D-1D hybrid nanochannels further reaches to 10^{12} cm^{-2} (VI). (**D**) *I-V* curves of the nanochannel membranes (at 0.1 M solution) before and after h-PEI modification. The symmetric SA nanochannels show a linear feature, while the h-PEI–capped nanochannels exhibit a diode-like feature, with the rectification ratio of 17.3. (**E**) Numerical simulation results for the ionic concentration distribution for an asymmetric nanochannel, showing the accumulation (at +2 V) and depletion (at −2 V) of ions along the axial position.

comparison between the asymmetric nanochannels and symmetric nanochannels is around 17.3, in agreement with the theoretically estimated number of equivalent nanochannels on the caps.

The ionic rectification property is quantitatively supported by a numerical simulation based on Poisson-Nernst-Planck equations (*29*). To simplify the analysis, we take one 1D-1D hybrid nanochannel as the model (Fig. 2E). From the ion concentration profile along the axis, we can see ions enrichment zone under positive bias and ion depletion zone under negative bias, which is in well agreement with the experiment result of Fig. 2D.

The unidirectional ion regulation ability maintains over a wide range of salinity concentrations from the *I-V* curves (Fig. 3, A and B). The rectification ratio varies as the concentration changes and shows the highest value in 0.1 M solution. The currents are still rectified

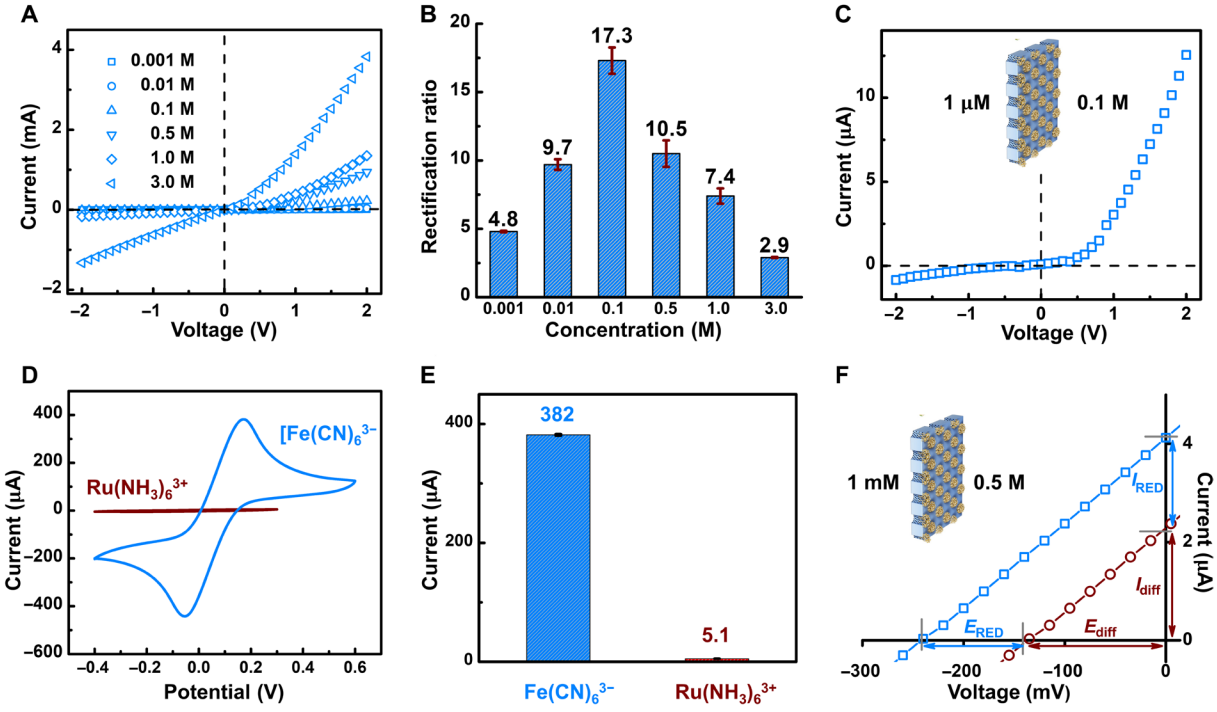

Fig. 3. The ion transport regulation of the nanochannel array membrane. (**A**) *I-V* curves obtained over a wide salinity concentration range. The ionic current values at positive potentials are substantially higher than those at negative potentials. (**B**) Corresponding rectification ratios at different concentrations, indicating excellent ion transport regulation over a wide range of concentrations. (**C**) *I-V* curve for an extremely high salinity gradient (1 μM/0.1 M), showing excellent Cl^- ion selectivity. (**D**) CV curves of the membrane when using $[Fe(CN)_6]^{3-}$ as the cationic electroactive probe and $[Ru(NH_3)_6]^{3+}$ as the anionic electroactive probe. (**E**) Peak currents of the CV curves when using $[Fe(CN)_6]^{3-}$ and $[Ru(NH_3)_6]^{3+}$ probes. (**F**) *I-V* curves of the membrane at 1 mM/0.5 M gradient, with the high-concentration solution on the cap side.

even in 3.0 M solution. These properties promise applications involving various water resources.

Excellent ion selectivity

The ultrahigh-density nanochannel membrane also exhibits excellent ion selectivity, which is essential for energy conversion. To verify the ion selectivity, the ion transport through the membrane is measured using highly asymmetric concentrations (*30*). The concentration on the cap side is 0.1 M, and the concentration on the other side is 1 μM. The concentration gradient ratio is up to 10^5. Thus, the ion migration contribution to the measured ionic current from the low concentration side is negligible. The ionic currents carried separately by cations and anions from the high concentration side are compared (Fig. 3C). The currents at positive potentials (Cl^-) are substantially higher than the currents at negative potentials (K^+), indicating the strong anion selectivity. The h-PEI caps at the entryway of the nanochannel array play a role similar to that of the Cl^- selectivity filter in Cl^- channels (*15*, *18*). The high content of positive-charged nitrogen atoms in h-PEI offers numerous coordinating sites for Cl^- ions, markedly decreasing the internal resistance. These structural and chemical properties favor a high Cl^- throughput. Meanwhile, the counterions, such as K^+ ions, are effectively prevented by the Donnan effect. The excellent anion selectivity can also be determined by a cyclic voltammetry (CV) test in the presence of electroactive redox probes, $[Fe(CN)_6]^{3-}$ and $[Ru(NH_3)_6]^{3+}$ (Fig. 3, D and E). The CV curves show a high electrochemical response with a peak current of 382 μA using $[Fe(CN)_6]^{3-}$ while a weak response with a peak current of 5.1 μA using $[Ru(NH_3)_6]^{3+}$. The marked contrast results from the preferential anion diffusion. Only the anions selectively transport toward the electrode through the h-PEI–capped nanochannels.

Moreover, the Cl^- ion selectivity is quantitatively expressed by the ion selectivity coefficient (*S*, equals 1 for ideal selectivity and 0 for nonselectivity), which can be calculated from the following equation (*31*, *32*)

$$S = \frac{E_{diff}}{\frac{RT}{F}\ln\left(\frac{\alpha_{KCl}^{HC}}{\alpha_{KCl}^{LC}}\right)} \quad (3)$$

where E_{diff} is the diffusion potential. *R*, *T*, and *F* are the universal gas constant, the temperature, and the Faraday constant, respectively, while α_{KCl}^{HC} and α_{KCl}^{LC} are the activities of the Cl^- in the high-concentration and low-concentration solutions. At a concentration gradient of 500-fold, the open-circuit voltage (U_{OC} = 241.3 mV) and short-circuit current (I_{SC} = 4.0 μA) of the hybrid membrane are obtained from the *I-V* curve. After subtracting the redox potential of the base window, the open-circuit voltage of the nanochannel array membrane is approximately 136.5 mV, and the diffusion current reaches 2.3 μA (Fig. 3F). The calculated *S* is ~0.91, suggesting excellent anion selectivity. The high ion selectivity of the membrane would benefit the high efficiency energy conversion.

Ultrahigh osmotic energy conversion

The energy conversion ability of the mushroom-shaped nanochannel array membrane is systematically researched. First, we explored

the current density and power density of the membrane as functions of external resistance and concentration gradient. Considering that the salinity concentration of sea water is around 0.5 M, the high-salinity solution with 0.5 M KCl is placed on the cap side, and the low-salinity solution is varied from 1 mM to 0.1 M with gradient ratios of 5, 50, and 500 (Fig. 4, A to C). The current densities decrease with load resistance increasing (Fig. 4A). The electric power (P_R) is directly obtained from $P_R = I^2 \times R_M$, where I is the generated current and R_M is the membrane resistance. When a load resistance (R_L) is connected to extract the generated power, the maximum extractable power reaches its maximum when $R_L = R_M$. The output power density increases with the salinity gradient and reaches a maximum of 22.4 W·m^{-2} for a 500-fold salinity gradient. The energy conversion system shows excellent endurance. The output power density maintains nearly unchanged within 2 weeks (fig. S14). Besides, the asymmetric membrane also presents pretty high performance using NaCl solution (fig. S15). Considering that the concentration of salt lakes is even higher, the energy conversion ability is evaluated using higher salinity solution (Fig. 4D and fig. S16). With the increasing salinity gradient, the power density increases and reaches an even higher value of 33.2 W·m^{-2} for a 1000-fold salinity gradient. In addition, the performance of the membrane for a 50-fold NaCl gradient and real seawater/river water is determined, and the power density is up to 13.2 and 14.6 W·m^{-2}, respectively (Fig. 4E and fig. S17), much higher than those of traditional ion-exchange membranes (*33*). The traditional ion-exchange membranes show really high area resistance and thus poor power density (*34*). Even for the symmetric BCP nanochannel array membrane, the power density is one order lower (fig. S18), due to the severe concentration polarization (*35*–*37*). The numerical simulation results show that the counterion concentration at the channel outlet is much higher than that of the bulk solution (fig. S19A). On the contrary, for the asymmetric membrane with dipolar charge distribution, the counterion (Cl^-) concentration at the channel outlet is much lower than the bulk value, indicating that the counterions are depleted (fig. S19B). Thus, the concentration polarization at the low concentration side is highly suppressed, contributing to the ultrahigh power density of the mushroom-shaped nanochannel array membrane. As shown in fig. S20, the current values increase as the number of cap nanochannels increases by numerical simulation. Notably, the economic cost is a crucially important factor for the industrial prospect. The cost is calculated to be about 3 USD·m^{-2} (fig. S21), which is quite lower than the commercially accepted target (4.8 USD·m^{-2}) (*38*). Thus, it promises a substantial payback by applying the designed membrane for osmotic energy conversion.

Next, we proceed to demonstrate the influence of membrane thickness on power density. The results present that the thinner the membrane is, the better performance it exhibits (Fig. 4F and fig. S22). It is mainly because the BCP nanochannel length decrease leads to the resistance decrease. It is worth noting that the ion selectivity, determined by the selective layer, is independent of the BCP nanochannel length. The numerical simulation shows that the current values decrease as the membrane thickness increases (fig. S23). For its excellent mechanical strength, the minimal thickness of the free-standing nanochannel array membrane is as thin as 118 nm in contrast to those

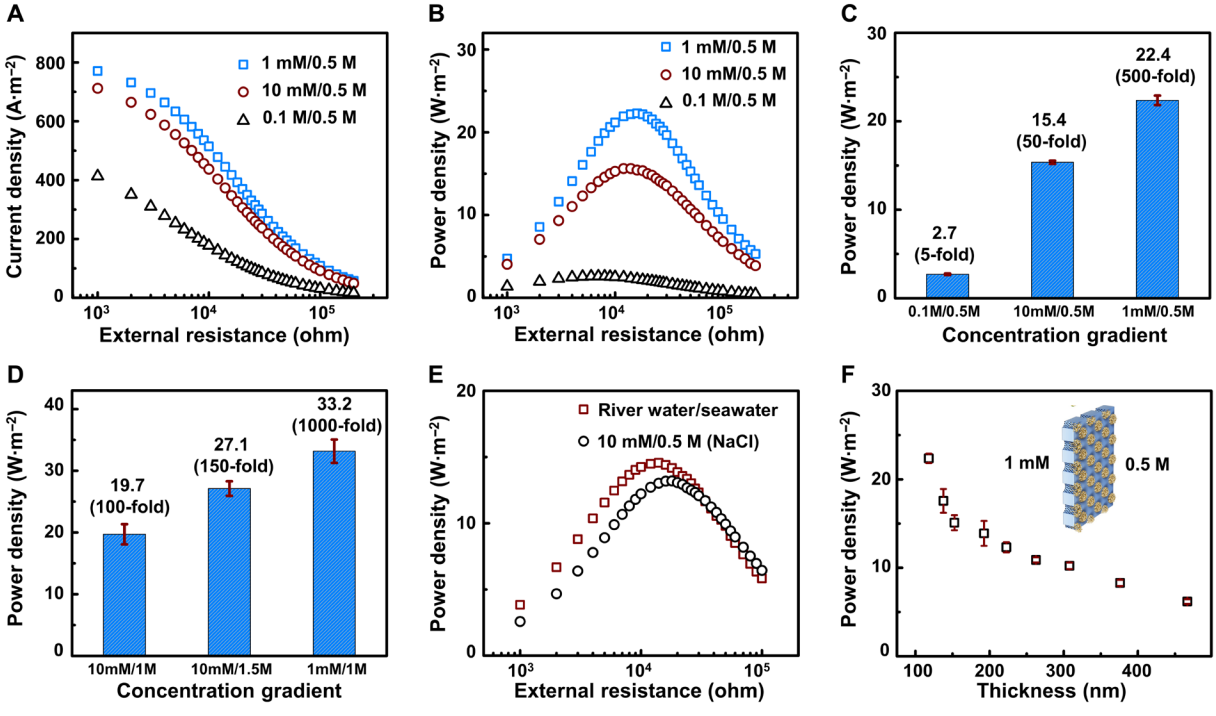

Fig. 4. The ultrahigh osmotic energy conversion. (**A**) The current densities at different concentration folds as a function of the external resistance. (**B**) The power densities at different concentration folds as a function of the external resistance. (**C**) The maximum output power densities at different concentration folds. The high-salinity solution placed on the cap side is fixed at 0.5 M KCl, and the low-salinity solution is varied from 1 mM to 0.1 M. The maximum value is 22.4 W·m^{-2}. (**D**) The maximum output power densities using high-salinity solutions. The maximum value reaches 33.2 W·m^{-2} for a 1000-fold salinity gradient. (**E**) The power densities obtained by using natural seawater and river water (□) and 10 mM/0.5 M NaCl solution (○). (**F**) The maximum output power density at 500-fold as a function of membrane thickness, showing that the power density increases as the membrane thickness decreases.

of the BNMs, which are usually in the range of micrometers. The design strategy overcomes the contradiction between pore density and mechanical strength. With pore density several orders higher, the output power density is much higher compared with upscaled membranes over a wide range of pore densities (table S1). By decreasing the BCP molecular weight, the areal density of the nanochannels could increase one order higher, up to ~10^{12} cm^{-2}. In this case, the estimated power density would reach ~10^2 $W{\cdot}m^{-2}$. Furthermore, we are designing a continuous manufacturing process of a 25-cm-wide membrane, which would provide the prospect for industrial application.

DISCUSSION

Here, we have demonstrated an ultrahigh-density mushroom-shaped nanochannel array membrane, generating the power density up to 22.4 $W{\cdot}m^{-2}$ for a 500-fold salinity gradient and an even higher value of 33.2 $W{\cdot}m^{-2}$ for a 1000-fold salinity gradient, which is the best performance among the upscaled membranes. The explanation considers the ultrathin selective layer and ultrahigh density of nanochannels. The mushroom-shaped nanochannels are formed by way of single-molecule–layer h-PEI capping the BCP-derived nanochannels. The negative-charged stem parts have a density of ~10^{11} cm^{-2}, while the positive-charged cap part is 3D channel networks, equivalent to tens of 1D nanochannels per stem. Thus, the total density of the asymmetric nanochannel reaches up to ~10^{12} cm^{-2}. The extremely high density of ion channels exhibits unidirectional ion transport and excellent ion selectivity, leading to high-performance energy conversion. Besides, the controlled process of membrane fabrication provides a promising approach for industrial production. This work represents a significant step toward developing the next generation of asymmetric nanopore membranes and opens up a promising prospect for large-scale osmotic energy conversion.

MATERIALS AND METHODS

Fabrication of the BCP SA membrane

Ten milligrams of BCP was dissolved in 0.5 ml of toluene and the solution was filtered. Four weight % poly(styrene sulfonic acid) sodium salt (PSS) aqueous solution was spin-coated onto silicon wafer at 2000 rpm for 120 s. Then, the BCP solution was spin-coated onto the PSS layer at 2000 rpm for 60 s. The prepared sample was dried in a nitrogen atmosphere for 2 hours. Then, the sample was annealed at 80°C for 6 hours.

Fabrication of the nanochannel membrane

The SA membrane was exposed under UV radiation (λ_{max} = 365 nm) for 30 min and then rinsed into methanol solution for 30 min to remove the polyethylene oxide.

Fabrication of the h-PEI–capped membrane

h-PEI (0.3 g), 0.005 g (0.026 mmol) of 1-ethyl-3-(3-dimethylaminopropyl)carbodiimide, and 0.001 g (0.008 mmol) of 4-dimethylaminopyridine were dissolved in 10 ml of ethanol, and then the solution was filtered. The filtered solution was spin-coated onto the nanochannel membrane at 3000 rpm for 120 s and stored under N_2 atmosphere at 40°C overnight. Then, the membrane was washed with ethanol for several times to remove the unmodified h-PEI. Then, the sample was immersed into the water to dissolve the PSS sacrificial layer. The free-standing h-PEI–capped membrane was obtained.

SUPPLEMENTARY MATERIALS

Supplementary material for this article is available at http://advances.sciencemag.org/cgi/content/full/7/21/eabg2183/DC1

REFERENCES AND NOTES

1. B. E. Logan, M. Elimelech, Membrane-based processes for sustainable power generation using water. *Nature* **488**, 313–319 (2012).
2. N. Y. Yip, D. Brogioli, H. V. M. Hamelers, K. Nijmeijer, Salinity gradients for sustainable energy: Primer, progress, and prospects. *Environ. Sci. Technol.* **50**, 12072–12094 (2016).
3. A. Siria, M.-L. Bocquet, L. Bocquet, New avenues for the large-scale harvesting of blue energy. *Nat. Rev. Chem.* **1**, 0091 (2017).
4. W. Guo, L. Cao, J. Xia, F. Nie, W. Ma, J. Xue, Y. Song, D. Zhu, Y. Wang, L. Jiang, Energy harvesting with single-ion–selective nanopores: A concentration gradient–driven nanofluidic power source. *Adv. Funct. Mater.* **20**, 1339–1344 (2010).
5. A. Siria, P. Poncharal, A. L. Biance, R. Fulcrand, X. Blase, S. T. Purcell, L. Bocquet, Giant osmotic energy conversion measured in a single transmembrane boron nitride nanotube. *Nature* **494**, 455–458 (2013).
6. J. Feng, M. Grafl, K. Liu, D. Ovchinnikov, D. Dumcenco, M. Heiranian, V. Nandigana, N. R. Aluru, A. Kis, A. Radenovic, Single-layer MoS_2 nanopores as nanopower generators. *Nature* **536**, 197–200 (2016).
7. C. Lin, C. Combs, Y. Su, L.-H. Yeh, Z. S. Siwy, Rectification of concentration polarization in mesopores leads to high conductance ionic diodes and high performance osmotic power. *J. Am. Chem. Soc.* **141**, 3691–3698 (2019).
8. M. Macha, S. Marion, V. V. R. Nandigana, A. Radenovic, 2D materials as an emerging platform for nanopore-based power generation. *Nat. Rev. Mater.* **4**, 588–605 (2019).
9. X. Liu, M. He, D. Calvani, H. Qi, K. B. S. S. Gupta, H. J. M. de Groot, G. J. A. Sevink, F. Buda, U. Kaiser, G. F. Schneider, Power generation by reverse electrodialysis in a single-layer nanoporous membrane made from core–rim polycyclic aromatic hydrocarbons. *Nat. Nanotechnol.* **15**, 307–312 (2020).
10. X. Zhu, J. Hao, B. Bao, Y. Zhou, H. Zhang, J. Pang, Z. Jiang, L. Jiang, Unique ion rectification in hypersaline environment: A high-performance and sustainable power generator system. *Sci. Adv.* **4**, eaau1665 (2018).
11. J. Gao, W. Guo, D. Feng, H. Wang, D. Zhao, L. Jiang, High-performance ionic diode membrane for salinity gradient power generation. *J. Am. Chem. Soc.* **136**, 12265–12272 (2014).
12. Z. Zhang, X. Sui, P. Li, G. Xie, X. Y. Kong, K. Xiao, L. Gao, L. Wen, L. Jiang, Ultrathin and ion-selective Janus membranes for high-performance osmotic energy conversion. *J. Am. Chem. Soc.* **139**, 8905–8914 (2017).
13. D. A. Doyle, J. M. Cabral, R. A. Pfuetzner, A. Kuo, J. M. Gulbis, S. L. Cohen, B. T. Chait, R. MacKinnon, The structure of the potassium channel: Molecular basis of K^+ conduction and selectivity. *Science* **280**, 69–77 (1998).
14. Y. Zhou, J. H. Morais-Cabral, A. Kaufman, R. MacKinnon, Chemistry of ion coordination and hydration revealed by a K^+ channel–Fab complex at 2.0-Å resolution. *Nature* **414**, 43–48 (2001).
15. R. Dutzler, E. B. Campbell, M. Cadene, B. T. Chait, R. MacKinnon, X-ray structure of a ClC chloride channel at 3.0 Å reveals the molecular basis of anion selectivity. *Nature* **415**, 287–294 (2002).
16. R. Dutzler, E. B. Campbell, R. MacKinnon, Gating the selectivity filter in ClC chloride channels. *Science* **300**, 108–112 (2003).
17. C. Miller, ClC chloride channels viewed through a transporter lens. *Nature* **440**, 484–489 (2006).
18. M. Pusch, U. Ludewig, A. Rehfeldt, T. J. Jentsch, Gating of the voltage-dependent chloride channel ClC-0 by the permeant anion. *Nature* **373**, 527–531 (1995).
19. D. A. Neamen, *Semiconductor Physics and Devices Basic Principles* (McGraw-Hill, ed. 4, 2011).
20. T. B. H. Schroeder, A. Guha, A. Lamoureux, G. VanRenterghem, D. Sept, M. Shtein, J. Yang, M. Mayer, An electric-eel–inspired soft power source from stacked hydrogels. *Nature* **552**, 214–218 (2017).
21. X. Sui, Z. Zhang, Z. Zhang, Z. Wang, C. Li, H. Yuan, L. Gao, L. Wen, X. Fan, L. Yang, X. Zhang, L. Jiang, Biomimetic nanofluidic diode composed of dual amphoteric channels maintains rectification direction over a wide pH range. *Angew. Chem. Int. Ed.* **55**, 13056–13060 (2016).
22. G. E. Ham, E. J. Goethals, *Polymeric Amines and Ammonium Salts*, E. J. Goethals, Ed. (Pergamon Press, 1980).
23. H. Ge, C. Wu, Separation of linear and star chains by a nanopore. *Macromolecules* **43**, 8711–8713 (2010).
24. O. V. Borisov, A. A. Darinskii, E. B. Zhulina, Stretching of polyelectrolyte coils and globules in an elongational flow. *Macromolecules* **28**, 7180–7187 (1995).
25. M. Rubinstein, R. H. Colby, *Polymer Physics* (Oxford Univ. Press, 2003).
26. C. B. Picallo, S. Gravelle, L. Joly, E. Charlaix, L. Bocquet, Nanofluidic osmotic diodes: Theory and molecular dynamics simulations. *Phys. Rev. Lett.* **111**, 244501 (2013).

27. R. B. M. Schasfoort, S. Schlautmann, J. Hendrikse, A. van den Berg, Field-effect flow control for microfabricated fluidic networks. *Science* **286**, 942–945 (1999).
28. I. Vlassiouk, S. Smirnov, Z. S. Siwy, Nanofluidic ionic diodes. Comparison of analytical and numerical solutions. *ACS Nano* **2**, 1589–1602 (2008).
29. D. Constantin, Z. S. Siwy, Poisson-Nernst-Planck model of ion current rectification through a nanofluidic diode. *Phys. Rev. E* **76**, 041202 (2007).
30. Y. He, D. Gillespie, D. Boda, I. Vlassiouk, R. S. Eisenberg, Z. S. Siwy, Tuning transport properties of nanofluidic devices with local charge inversion. *J. Am. Chem. Soc.* **131**, 5194–5202 (2009).
31. I. Vlassiouk, S. Smirnov, Z. Siwy, Ionic selectivity of single nanochannels. *Nano Lett.* **8**, 1978–1985 (2008).
32. D.-K. Kim, C. Duan, Y.-F. Chen, A. Majumdar, Power generation from concentration gradient by reverse electrodialysis in ion-selective nanochannels. *Microfluid. Nanofluid.* **9**, 1215–1224 (2010).
33. M. Tedesco, A. Cipollina, A. Tamburini, G. Micale, Towards 1 kW power production in a reverse electrodialysis pilot plant with saline waters and concentrated brines. *J. Membr. Sci.* **522**, 226–236 (2017).
34. J. Hong, B. Zhang, S. Glabman, N. Uzal, X. Dou, H. Zhang, X. Wei, Y. Chen, Potential ion exchange membranes and system performance in reverse electrodialysis for power generation: A review. *J. Membr. Sci.* **486**, 71–88 (2015).
35. J. W. Post, H. V. M. Hamelers, C. J. N. Buisman, Energy recovery from controlled mixing salt and fresh water with a reverse electrodialysis system. *Environ. Sci. Technol.* **42**, 5785–5790 (2008).
36. Q. Pu, J. Yun, H. Temkin, S. Liu, Ion-enrichment and ion-depletion effect of nanochannel structures. *Nano Lett.* **4**, 1099–1103 (2004).
37. S. J. Kim, Y.-C. Wang, J. H. Lee, H. Jang, J. Han, Concentration polarization and nonlinear electrokinetic flow near a nanofluidic channel. *Phys. Rev. Lett.* **99**, 044501 (2007).
38. A. Daniilidis, R. Herber, D. A. Vermaas, Upscale potential and financial feasibility of a reverse electrodialysis power plant. *Appl. Energy* **119**, 257–265 (2014).
39. T. Gao, T. Wang, W. Wu, Y. Liu, Q. Huo, Z. Qiao, S. Dai, Solvent-induced self-assembly strategy to synthesize well-defined hierarchically porous polymers. *Adv. Mater.* **31**, 1806254 (2019).
40. S. H. Kwak, S. R. Kwon, S. Baek, S. M. Lim, Y. C. Joo, T. D. Chung, Densely charged polyelectrolyte-stuffed nanochannel arrays for power generation from salinity gradient. *Sci. Rep.* **6**, 26416 (2016).
41. J. Ji, Q. Kang, Y. Zhou, Y. Feng, X. Chen, J. Yuan, W. Guo, Y. Wei, L. Jiang, Osmotic power generation with positively and negatively charged 2D nanofluidic membrane pairs. *Adv. Funct. Mater.* **27**, 1603623 (2017).
42. T. C. Tsai, C. W. Liu, R. J. Yang, Power generation by reverse electrodialysis in a microfluidic device with a nafion ion-selective membrane. *Micromachines* **7**, 205 (2016).
43. P. Długołęcki, J. Dąbrowska, K. Nijmeijer, M. Wessling, Ion-conductive spacers for increased power generation in reverse electrodialysis. *J. Membr. Sci.* **347**, 101–107 (2010).
44. J. Veerman, R. M. de Jong, M. Saakes, S. J. Metz, G. J. Harmsen, Reverse electrodialysis: Comparison of six commercial membrane pairs on the thermodynamic efficiency and power density. *J. Membr. Sci.* **343**, 7–15 (2009).
45. S. Balme, T. Ma, E. Balanzat, J. M. Janot, Large osmotic energy harvesting from functionalized conical nanopore suitable for membrane applications. *J. Membr. Sci.* **544**, 18–24 (2017).
46. Z. Zhang, X. Kong, K. Xiao, Q. Liu, G. Xie, P. Li, J. Ma, Y. Tian, L. Wen, L. Jiang, Engineered asymmetric heterogeneous membrane: A concentration-gradient-driven energy harvesting device. *J. Am. Chem. Soc.* **137**, 14765–14772 (2015).
47. R. Li, J. Jiang, Q. Liu, Z. Xie, J. Zhai, Hybrid nanochannel membrane based on polymer/MOF for high-performance salinity gradient power generation. *Nano Energy* **53**, 643–649 (2018).
48. W. Xin, Z. Zhang, X. Huang, Y. Hu, T. Zhou, C. Zhu, X. Kong, L. Jiang, L. Wen, High-performance silk-based hybrid membranes employed for osmotic energy conversion. *Nat. Commun.* **10**, 3876 (2019).

Acknowledgments: We thank S. Yang, Y. Jiang, and S. Qi for helpful discussion. We thank L. Luo for assistance with the TEM and Z. Liu and T. Sun for assistance with the AFM. **Funding:** This work is financially supported by the National Key Research and Development Program of China (2017YFA0206904, 2017YFA0206900, and 2016YFC1402500), the National Natural Science Foundation of China (21875009), and the Fundamental Research Funds for the Central Universities. **Author contributions:** L.G. and L.J. conceived the idea and designed all experiments. L.W. discussed the results and provided constructive ideas. C.L. carried out all experiments with the help of X.S. and Y.C. All authors discussed the results and wrote the manuscript together. **Competing interests:** The authors declare that they have no competing interests. **Data and materials availability:** All data needed to evaluate the conclusions in the paper are present in the paper and/or the Supplementary Materials. Additional data related to this paper may be requested from the authors.

Submitted 17 December 2020
Accepted 29 March 2021
Published 19 May 2021
10.1126/sciadv.abg2183

Citation: C. Li, L. Wen, X. Sui, Y. Cheng, L. Gao, L. Jiang, Large-scale, robust mushroom-shaped nanochannel array membrane for ultrahigh osmotic energy conversion. *Sci. Adv.* **7**, eabg2183 (2021).